MATERIALS CHEMISTRY FRONTIERS

RESEARCH ARTICLE

View Article Online
View Journal | View Issue

Cite this: *Mater. Chem. Front.*, 2023, **7**, 3164

Zero-dimensional indium hybrids and modulated photoluminescence by Sb doping†

Chen Fang,[a] Yingjie Mao,[a] Guojun Zhou,[b] Zhichao Zhang,[c] Yaohui Zhu,[a] Denghui Xu,[a] Xiong Li,[a] Aicong Geng[a] and Jun Zhou*[a]

Received 27th February 2023,
Accepted 26th April 2023

DOI: 10.1039/d3qm00211j

rsc.li/frontiers-materials

Zero-dimensional (0D) indium hybrids have been recently explored as promising platforms for use in solid-state lighting owing to their environmental friendliness and stability. Herein, we first designed a novel 0D indium hybrid $(TEA)_2InCl_5$ (tetraethylammonium$^+$, $C_8NH_{20}^+$), where the organic cation $(TEA)^+$ cocrystallizes with five-coordinated $[InCl_5]^{2-}$ square pyramids. Experimental data and first-principles calculations reveal that the blue emissions are attributed to the organic cations $(TEA)^+$ and self-trapped excitons (STEs) in the inorganic $[InCl_5]^{2-}$ square pyramids. Remarkably, when incorporating Sb^{3+} ions, the value of photoluminescence quantum yield (PLQY) is greatly enhanced to 78.85%, and the emission color could be tuned from blue to warm white and finally to orange-red. This success of $(TEA)_2InCl_5:Sb^{3+}$ not only enriches the structure and optical properties of 0D indium hybrids, but also provides a new direction towards modulating the optical performance through a doping strategy.

Introduction

Zero-dimensional (0D) organic–inorganic metal halide hybrids (OIMHs), whose inorganic metal halide units are totally isolated from each other by large organic cations, have become star materials in the fields of optoelectronics.[1] On the one hand, the lowest dimensionality enables the softest lattice and strongest quantum confinement effect as well as the strongest electron–phonon interaction, resulting in self-trapped excitons (STEs) and efficient broadband emissions with large Stokes shifts.[2,3] On the other hand, the unique 'host–guest' structure makes it possible for multiple metal halide species to coexist in the same structure, which presents a highly promising direction towards obtaining multifunctional materials.[4,5]

Recently, a large number of 0D OIMHs based on lead, tin, germanium, antimony, bismuth, indium, manganese, and others have been widely developed as candidate materials for solid-state light-emitting areas.[6] Compared with the toxicity of Pb^{2+} as well as instabilities of Sn^{2+} and Ge^{2+}, In^{3+}-based OIMHs with lone-pair-free metal cations have been rapidly developed benefitting from the environmental friendliness and stability. Up to now, about 20 0D In-based OIMHs have been reported, which show a variety of inorganic building blocks including tetrahedral $[InX_4]^-$, pyramidal $[InX_5]^{2-}$, octahedral $[InX_6]^{3-}$, and dimeric $[In_2X_{10}]^{4-}$ (Table S1, ESI†).[7] Most of these 0D In-based OIMHs exhibit orange-red broadband emission originating from the intrinsic STEs due to the large excited-state structural distortion of isolated $[InX_6]^{3-}$ octahedrons,[8,9] while $[InX_4]^-$ tetrahedrons are only used as the anionic spacer to stabilize the crystal structure and have little contribution to the optical properties.[10,11] However, the In-based OIMHs with $[InX_5]^{2-}$ square pyramids and higher energy emission are largely unexplored. To our knowledge, among the reported five-coordinated In-based OIMHs, only $(C_{13}H_{14}N)_2InCl_5$ shows blue emission with a photoluminescence quantum yield (PLQY) of 5.44%, while $(C_{20}H_{20}P)_2InCl_5$ and $(C_6H_{18}N_2)InCl_5{\cdot}H_2O$ hardly exhibit emission.[12–14] Hence, the development of 0D In-based OIMHs with $[InX_5]^{2-}$ square pyramids and higher energy emission is beneficial to enrich the structure and luminescence of indium hybrids.

Herein, we report a novel 0D OIMH with the formula of $(TEA)_2InCl_5$, where the isolated $[InCl_5]^{2-}$ square pyramids are completely separated and embedded periodically in the large organic cations $(TEA)^+$. Experimental data and theoretical calculation reveal that both the STEs in the inorganic $[InCl_5]^{2-}$ square pyramids and organic cations $(TEA)^+$ contribute to luminescence. In addition, since doping trivalent antimony (Sb^{3+}) ions in 0D OIMHs has been regarded as an efficient strategy towards regulating the emission color and enhancing emission intensity,

[a] *Department of Physics, Beijing Technology and Business University, Beijing 100048, China. E-mail: jzhou1204@btbu.edu.cn*
[b] *Laboratory of Magnetic Molecules and Magnetic Information Materials (Ministry of Education), School of Chemistry and Material Science, Shanxi Normal University, Taiyuan 030031, China*
[c] *Energy Materials and Low-carbon Technology Research Institute, Department of Energy Chemistry and Materials Engineering, ShanXi Institute of Energy, Jinzhong 030600, China*

† Electronic supplementary information (ESI) available. CCDC 2244814. For ESI and crystallographic data in CIF or other electronic format see DOI: https://doi.org/10.1039/d3qm00211j

we fabricated a series of $(TEA)_2InCl_5:Sb^{3+}$ to investigate the effects of replacing $[InCl_5]^{2-}$ square pyramids by $[SbCl_5]^{2-}$ square pyramids on the crystal structure and luminescence properties.[15] After doping Sb^{3+}, the emission color could be tuned from blue to warm white and finally to orange-red, and the value of PLQY is greatly improved from 30.11% to 78.85%. The design rule established here will provide insights towards generating efficient multiple emissions in 0D metal halides for varied applications in the future.

Experimental

Materials and preparation

All the chemicals were commercially purchased and used without further purification. Tetraethylammonium chloride (TEAC) (99%), indium chloride tetrahydrate ($InCl_3{\cdot}4H_2O$) (99.9%), antimony chloride ($SbCl_3$) (99.99%), and *N*,*N*-dimethylformamide (DMF) (99.9%) were purchased from Aladdin Co. Ltd. (Shanghai, China) and used without further purification. $(TEA)_2InCl_5$ single crystals were prepared as follows: TEAC and $InCl_3$ were dissolved in DMF under heating and continuous stirring at 343 K. The crystals were obtained by slowly cooling the saturated solution to room temperature with a controlled cooling rate to obtain the crystals. The synthetic route for Sb-doped samples was similar to that of the pure $(TEA)_2InCl_5$ with $SbCl_3$ added for the targeted compositions.

Measurements and characterization

The diffraction patterns of $(TEA)_2InCl_5$ single crystals were obtained using a Bruker APEX-II CCD diffractometer at 150 K with a Mo-Kα (λ = 0.71073 Å) radiation source. The powder X-ray diffraction (PXRD) patterns were examined with a Germanic model D2 PHASER (Bruker, Karlsruhe) using Cu-Kα radiation (λ = 0.1506 Å), which was operated at 30 kV and 10 mA. The inductively coupled plasma optical emission spectrometry (ICP-OES) measurements were recorded on an Agilent ICP-OES 725 ES. The absorption spectrum was measured at room temperature using a Varian Cary 5 ultraviolet-visible-near infrared spectrophotometer. The room-temperature emission spectra (PL) and excitation spectra (PLE) were recorded using an FS5 fluorescence spectrophotometer (Edinburgh Instruments Ltd., U.K.). The decay curves were also recorded on the FS5, where the nanosecond decay curves were achieved using 365 nm pulse laser radiation as the excitation source. Temperature-dependent luminescence properties were measured using the FS5, where a liquid nitrogen cryostat on Oxford Instruments attached to the FS5 was used for low temperature measurements and connected heating equipment was used for high temperature measurements. The PLQY was obtained by incorporating an integrating sphere into a Nanolog fluorescence spectrometer (HORIBA Scientific, U.S.). Thermogravimetric analysis (TGA) was performed on a TGA55 thermal analyzer system at 10 °C min^{-1} in an argon flow from room temperature to 1000 °C.

Computational details

Our first-principles calculations were carried out within the framework of Density Functional Theory (DFT) as implemented in the Vienna Ab initio Simulation Package (VASP). The Perdew–Burke–Ernzerhof (PBE) functional[16] was chosen among the functionals available in the pseudopotentials generated by the projector augmented wave (PAW) method.[17,18] The DFT-D3 method with the Becke–Johnson damping was used to take into account the van der Waals (vdW) dispersion energy correction.[19,20] Moreover, the cutoff energy was set to be 520 eV, and the crystal structure was optimized until the forces acting on each atom is smaller than 0.01 eV $Å^{-1}$ with the fixed cell shape (determined by experiments). The *k*-mesh of 5 × 5 × 3 was used for crystal structure optimization, and then it was increased to 7 × 7 × 5 for self-consistent calculations as well as the determination of density of states (DOS). Finally, we used VASPKIT, which is a postprocessing tool for the VASP.[21]

Results and discussion

Well-formed bulky single crystals of $(TEA)_2InCl_5$ were synthesized *via* a solution method, which exhibited blue light under 365 nm UV light. Single-crystal X-ray diffraction (SCXRD) at 150 K was used to determine the crystal structure of $(TEA)_2InCl_5$, and the crystallographic information file (CIF) of $(TEA)_2InCl_5$ is demonstrated in the ESI.† $(TEA)_2InCl_5$ crystallizes in the tetragonal *P*4/*n* space group with the cell parameters of $a = b =$ 9.2680 Å, c = 14.0369 Å, and $\alpha = \beta = \gamma = 90°$. More detailed data of crystal diffraction refinements are summarized in Table S2 (ESI†). As shown in Fig. 1a, $(TEA)_2InCl_5$ exhibits a perfect 0D structure, where the isolated $[InCl_5]^{2-}$ square pyramids are

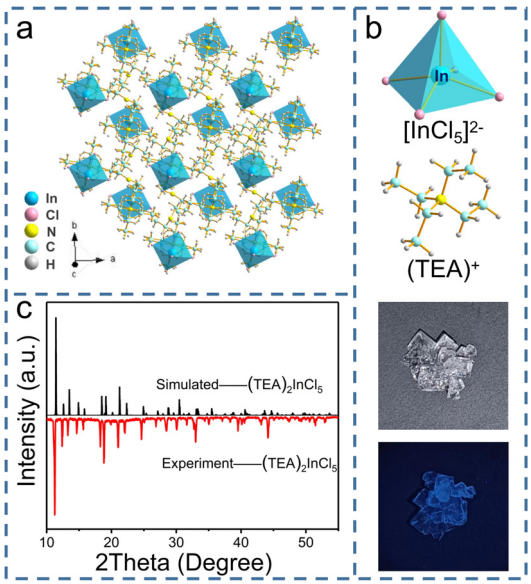

Fig. 1 (a) Crystal structure of the 0D $(TEA)_2InCl_5$. (b) Structures of an $[InCl_5]^{2-}$ square pyramid and organic cation $(TEA)^+$, as well as the photographs of single crystals under natural light and 365 nm UV light. (c) Comparison of experimental and simulated PXRD patterns of $(TEA)_2InCl_5$.

completely separated from each other and embedded periodically in the large organic cations $(TEA)^+$. Significantly, there is only one type of In^{3+} site, which coordinated with five Cl^- anions forming the $[InCl_5]^{2-}$ square pyramids (Fig. 1b and Fig. S1, ESI†). The In–Cl bond length ranges from 2.419 Å to 2.458 Å in $[InCl_5]^{2-}$ and the Cl–In–Cl bond angle ranges from 86.89° to 103.46°. Furthermore, the distortion degree of the $[InCl_5]^{2-}$ square pyramids for $(TEA)_2InCl_5$ can be calculated based on In–Cl bonds and Cl–In–Cl angles by the following equations:[22]

$$\lambda = \frac{1}{5}\sum_{i=1}^{5}\left[\frac{d_i - d_0}{d_0}\right]^2$$

$$\sigma^2 = \frac{1}{7}\sum_{i=1}^{8}(\theta_i - 90^\circ)^2$$

where d_i is the five individual In–Cl bond lengths, d_0 is the length of the average In–Cl bond and θ_i is each of the Cl–In–Cl bond angles of the square pyramids. The calculation results of λ and σ^2 are 4.2×10^{-5} and 109.02, respectively, demonstrating the high distortion in $[InCl_5]^{2-}$ square pyramids. Moreover, the well-fitted PXRD patterns of simulated and experimental data indicate the high purity of the obtained compounds (Fig. 1c). Furthermore, TGA shows that the $(TEA)_2InCl_5$ crystal was stable up to 277 °C (Fig. S2, ESI†).

To investigate the electronic structures and photophysical properties, we performed first-principles calculations for $(TEA)_2InCl_5$. Fig. 2a shows that $(TEA)_2InCl_5$ has an indirect bandgap with a bandgap of 3.7 eV. The conduction band minimum (CBM) is located at point Γ, while the valence band maximum (VBM) is located at point A. Fig. 2b indicates that the VBM of $(TEA)_2InCl_5$ is dominated by $(TEA)^+$ p and Cl p orbitals, and the CBM is dominated by In s and Cl p orbitals. Moreover, the DOS of $(TEA)^+$ p orbitals is also noticeable at the CBM, and is dominant for the higher vacant bands starting roughly from 5.7 eV. Therefore, the inorganic $[InCl_5]^{2-}$ square pyramids might play a major role in the PL emission and the $(TEA)^+$ also contributes to luminescence.

In order to verify the luminescence origin of $(TEA)_2InCl_5$ obtained by theoretical calculations, the optical absorption spectrum, photoluminescence spectra and decay lifetimes were measured. As depicted in Fig. 3a, the absorption spectrum of $(TEA)_2InCl_5$ shows an abrupt absorption onset featured at around 236 nm originating from a spin-allowed transition, combined with a long weak absorption band tailed up to 800 nm, which is similar to other reported In-based OIMHs.[23] Besides, by extracting from the Tauc plot, the indirect optical band gap of $(TEA)_2InCl_5$ is calculated to be 4.39 eV, which is consistent with their colorless and transparent nature.

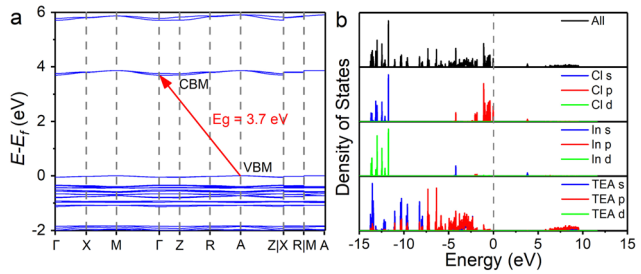

Fig. 2 (a) Calculated energy band structure. (b) The total and partial density of states of $(TEA)_2InCl_5$.

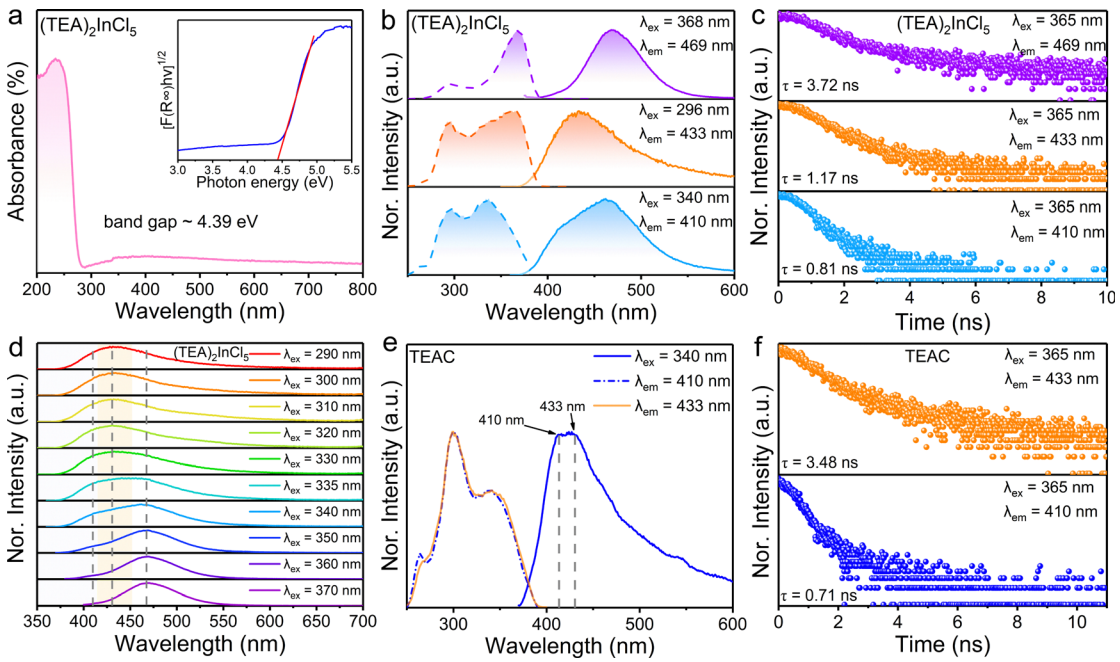

Fig. 3 (a) The absorption spectrum of $(TEA)_2InCl_5$. Inset: The Tauc plot showing the characteristics of the indirect band gap. (b) Room-temperature PLE and PL spectra of $(TEA)_2InCl_5$. (c) Room-temperature photoluminescence decay curves of $(TEA)_2InCl_5$. (d) Wavelength-dependent PL spectra of $(TEA)_2InCl_5$. (e) Room-temperature PLE and PL spectra of TEAC. (f) Room-temperature photoluminescence decay curves of TEAC.

Additionally, the experimental band gap is slightly larger than the calculated one because of the well-known underestimation of the bandgap by DFT calculation.[24,25]

As shown in Fig. 3b, the PLE spectrum of $(TEA)_2InCl_5$ monitored at 469 nm consists of two bands at around 296 nm and 368 nm. Under 368 nm irradiation, $(TEA)_2InCl_5$ exhibits a blue emission centered at 469 nm with a lifetime of 3.72 ns as well as a Stokes shift and full width at half maximum (FWHM) of 0.73 eV and 64 nm, respectively. While when excited at 296 nm, $(TEA)_2InCl_5$ displays an asymmetry emission band peaked at 433 nm with a short lifetime of 1.17 ns, whose PLE spectrum shows two new bands at 262 and 340 nm. Furthermore, upon 340 nm excitation, a new emission band with a lifetime of 0.81 ns appeared at 410 nm besides the 433 nm emission band. These spectral results are consistent with the wavelength-dependent PL spectra of $(TEA)_2InCl_5$ (Fig. 3d), suggesting that multiple luminescent centers existed in $(TEA)_2InCl_5$. To verify the origin of luminescence in $(TEA)_2InCl_5$ obtained by theoretical calculation, we performed comparative studies of the optical properties between $(TEA)_2InCl_5$ and the corresponding organic salt TEAC (Fig. 3e and f). Compared to $(TEA)_2InCl_5$, TEAC has the same emission bands at 410 nm and 433 nm, whose lifetimes are 0.71 ns and 3.48 ns, respectively. Moreover, the excitation peaks under 410 nm and 433 nm monitoring are totally consistent with that of $(TEA)_2InCl_5$. It is obvious that the photoluminescence of TEAC mainly depends on the π–π^* transition, and the recombination of different energy levels leads to multiple emission peaks.[26] Hence, combined with the results of DFT calculations, it can be understood that the emission peak centered at 410 nm and 433 nm are derived from the π–π^* transition in the organic cation $(TEA)^+$, while the emission peak at 469 nm might be ascribed to inorganic $[InCl_5]^{2-}$ units. This type of organic ion contributing to the PL has been reported in many 0D OIHMs, such as $RInBr_4$ (R = trimethyl(4-stilbenyl)-methylammonium), $(C_8NH_{12})_6InBr_9{\cdot}H_2O$, $BAPPIn_2Cl_{10}$ (BAPP = 1,4-bis(3-aminopropyl)piperazine) and so on.[27–29] It is noteworthy that the PLQY was determined to be 30.11% (excited by 368 nm), which is higher than those of the reported five-coordinated In-based metal halides (Table S1, ESI†), indicating that $(TEA)_2InCl_5$ has great application potential in the field of solid-state lighting.

In order to gain an insight into the photophysical mechanism of inorganic $[InCl_5]^{2-}$ units in $(TEA)_2InCl_5$, temperature-dependent photoluminescence excited at 368 nm was recorded from 140 K to 350 K. As shown in Fig. 4a, the emission intensity decreased gradually with increasing temperature, which is ascribed to the increased nonradiative recombination. To further investigate the thermal quenching process, the activation energy can be calculated using the Arrhenius function:[30]

$$I(T) = \frac{I_0}{A\exp\left(-\frac{E_a}{kT}\right)}$$

where I_T is the PL intensity at different temperatures, I_0 is the initial PL intensity, A is a constant, k is the Boltzmann constant, and E_a is the activation energy for thermal quenching. In general, the larger the E_a, the larger energy barrier that the electrons need to overcome from the excited state back to the ground state through the nonradiative transition. According to this function, two E_a values were observed, 0.256 eV (E_{a1}) at a high temperature and 0.044 eV (E_{a2}) at a low temperature, which demonstrates that there are two thermal processes in inorganic $[InCl_5]^{2-}$ units (Fig. 4b). Since E_{a1} is a thermal quenching phenomenon induced by the nonradiative transition at the intersection of the ground state and excited state, the high temperature process belongs to the thermal ionization process and the multiple thermal processes can be described using the following equation:[31]

$$I(T) = \frac{I_0}{1 + A_1\exp\left(-\frac{E_{a1}}{kT}\right) + A_2\exp\left(-\frac{E_{a2}}{kT}\right)}$$

On the other hand, the FWHM increases from 50 nm to 90 nm, which is attributed to the enhanced electron–phonon coupling effect with increasing temperature.[32] Temperature-dependent FWHM can be expressed using the formula:[33]

$$\mathrm{FWHM}(T) = 2.36\sqrt{S}\hbar\omega\sqrt{\coth\frac{\hbar\omega}{2kT}}$$

where S is the electron–phonon coupling parameter, $\hbar\omega$ is the phonon frequency, and k is the Boltzmann constant. Based on this equation, the values of S and $\hbar\omega$ were calculated to be 46.56 and 9.43 meV (Fig. 4c). Such a large S value not only indicates a strong electron–phonon coupling in the soft halide matrix, but also further proves that the blue broad emission at 469 nm in

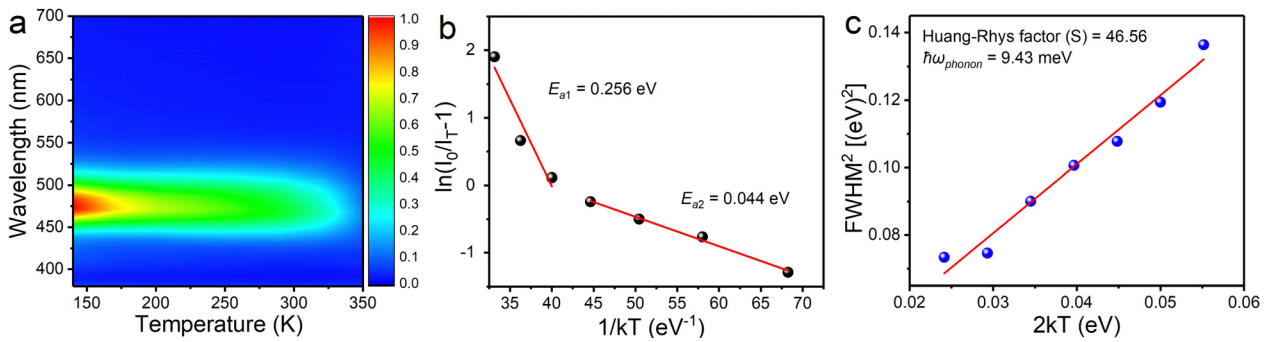

Fig. 4 (a) Temperature-dependent PL spectra of inorganic $[InCl_5]^{2-}$ units in $(TEA)_2InCl_5$ excited at 368 nm. (b) Plot of $\ln(I_0/I_T\text{-}1)$ *versus* $1/kT$ of $(TEA)_2InCl_5$. (c) Fitting results of $FWHM^2$ as a function of $2kT$.

$(TEA)_2InCl_5$ is attributed to STEs of $[InCl_5]$ units. In addition, the emission peak shows a slight blue shift owing to the lattice deformation and the change of the valence band with temperature, which is similar to $Cs_2Na_{0.75}Ag_{0.25}BiCl_6$ and Cs_2ZrCl_6:Tb^{3+}. The emission energy (E_{STEs}) of the STEs can be described by $E_{STEs} = E_g - E_b - E_{st} - E_d$, where E_g is the band gap energy, E_b is the exciton binding energy, E_{st} is the self-trapping energy, and E_d is the lattice deformation energy. The lattice deformation is slightly at low temperature but severely at high temperature, which causes the increase and decrease of the valence band, respectively. Such a unique band gap structure generated a larger E_{STEs} at high temperature for observing blue shift emission.[34,35]

Recently, dopants in metal halides provide a promising way for controlling the photoluminescence performances. Among the active ion doping procedures, Sb^{3+} ions with the electronic structure similar to In^{3+} ions have been regarded as effective optically active luminescent ions in metal halides. Hence, we have tried to replace $[InCl_5]^{2-}$ square pyramids by $[SbCl_5]^{2-}$ square pyramids to modulate the luminescence performance. As given in Fig. 5a, high quality single crystals are yielded, which exhibit bright orange-red emission, indicating a different photophysical mechanism from $(TEA)_2InCl_5$. Fig. 5b shows the PXRD patterns of as-synthesized $(TEA)_2In_{1-x}Cl_5:xSb^{3+}$ ($x = 0.05$, 0.1 and 0.3), together with a simulated pattern of $(TEA)_2InCl_5$. It can be found that all the diffraction peaks are well indexed to $(TEA)_2InCl_5$, suggesting that doping Sb^{3+} ions did not introduce impurities. However, for the PXRD pattern of sample $x = 0.4$, the impurity of $(TEA)_2SbCl_5$ occurred. In addition, ICP-OES was used to precisely determine the actual chemical composition of $(TEA)_2In_{1-x}Cl_5:xSb^{3+}$. For the feeding Sb concentrations (*i.e.*, the Sb/(Sb + In) molar ratio) being 5% and 30%, the ICP-OES-determined Sb concentrations are 10.9% and 46.9%, respectively. Hereafter, we denote the samples as $(TEA)_2In_{1-x}Cl_5:xSb^{3+}$ using the feeding concentration.

The photophysical properties of $(TEA)_2InCl_5:Sb^{3+}$ are fully characterized as discussed below. Sb^{3+} are typical ions with the outer electronic configuration of $5s^2$, which have the ground state of $^1S_0$ and their first excited state generally split into singlet state $^1P_1$ and triplet state ^3P_n ($n = 0$, 1 and 2). According to the transition rules, the transitions of $^1S_0$–$^3P_0$ and $^1S_0$–$^3P_2$ are totally forbidden at the electric dipole transition level but can be induced by lattice vibration, whereas the transition of $^1S_0$–$^1P_1$ is allowed and the $^1S_0$–$^3P_1$ transition is partially allowed due to spin–orbit coupling for heavy atoms.[36] Upon Sb doping, the absorption in the range of 320–440 nm is significantly enhanced, which is attributed to the more efficient absorption transition of Sb^{3+} with the $4d^{10}5s^25p^0$ configuration than that of In^{3+} with the $4d^{10}5s^05p^0$ configuration (Fig. 6a). The absorption at around 298 nm and 380 nm can be assigned to the $^1S_0$–$^1P_1$ and $^1S_0$–$^3P_1$ transition, respectively.[29] Fig. 6b and Fig. S3 (ESI†) show the PLE and PL spectra of $(TEA)_2In_{0.95}Cl_5:0.05Sb^{3+}$. In addition to the 469 nm and 410 nm emission bands attributed to $[InCl_5]^{2-}$ square pyramids and $(TEA)^+$, respectively, new dual-band emission appears with the peaks located at 500 nm and 660 nm with lifetimes of 9.76 ns and 5.45 μs, respectively (Fig. 6c), which are quite different from that of $(TEA)_2InCl_5$, indicating that the luminescence comes from the dopant Sb^{3+}. As is known, the most recognized luminescence mechanism of dual-emission in Sb-based metal halides is the ultrafast excited-state reorganization induced by the highly distorted $[SbCl_5]^{2-}$ square pyramids after the electrons reach the excited state through S–P transition, which finally leads to a high energy singlet STE emission with a short lifetime and a low energy triplet STE emission peak with a long lifetime.[37] Hence, the peaks at 500 nm and 660 nm are attributed to the characteristics of singlet STEs and triplet STEs of $[SbCl_5]^{2-}$ square pyramids, respectively. It is worth noting that there is no energy transfer process in $(TEA)_2InCl_5:Sb^{3+}$, but a mixture of luminescence from $[SbCl_5]^{2-}$ square pyramids and $[InCl_5]^{2-}$ square pyramids as well as $(TEA)^+$. The reasons are explained as follows: (1) the PLE spectra of Sb^{3+} monitored at 500 nm and 660 nm are quite different from $[InCl_5]^{2-}$ square pyramids and $(TEA)^+$, which is the most direct and fundamental evidence to prove that there is no energy transfer;[35] (2) there is little spectral overlap between the $(TEA)_2InCl_5$ PL and Sb^{3+} PLE spectrum.

With increasing Sb^{3+} concentration, the intensities of the new dual-band emission (500 and 660 nm) increase gradually, while those of $[InCl_5]^{2-}$ square pyramids and the organic cation $(TEA)^+$ gradually decrease (Fig. 6d). At the same time, the lifetime of $[InCl_5]^{2-}$ square pyramids monitored at 470 nm significantly increased from 3.73 ns to 18.25 ns (Fig. 6e). Both the PL spectra and lifetime results might be due to the increasing proportion of $[SbCl_5]^{2-}$ square pyramids and the stronger STE emission of $[SbCl_5]^{2-}$ square pyramids. Therefore, $(TEA)_2In_{0.7}Cl_5:0.3Sb^{3+}$ with a PLQY of 78.85% (excited by 340 nm) was selected as the studied composition of the potential red-emitting phosphor for the solid-state lighting field in the present series. The PLE and PL spectra of $(TEA)_2In_{0.7}Cl_5:0.3Sb^{3+}$ are presented in Fig. S4 and S5 (ESI†). When the excited wavelength increases from 280 nm to 380 nm, the emission intensity ratio of triplet STEs of $[SbCl_5]^{2-}$ square pyramids to the singlet STEs of $[SbCl_5]^{2-}$ square pyramids as well as STEs of $[InCl_5]^{2-}$ square pyramids firstly decreased and then increased, owing to the varying distribution of the photo-generated excitons. At the same time, tunable warm white emission can be obtained with correlated color temperatures (CCT) of up to 4054 K (Fig. 6f and Table S3, ESI†). In addition, warm white emission could also be achieved by adjusting the doping concentration of Sb^{3+}. Hence, doping Sb^{3+} ions and

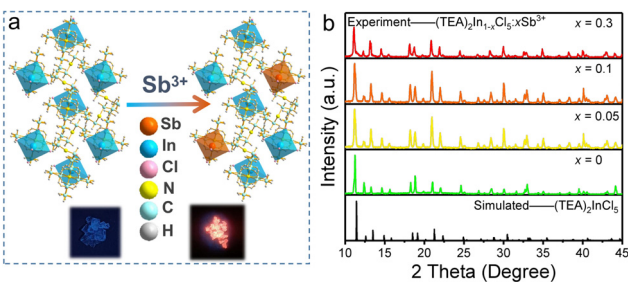

Fig. 5 (a) Doping mechanism and (b) PXRD patterns of $(TEA)_2In_{1-x}Cl_5:xSb^{3+}$.

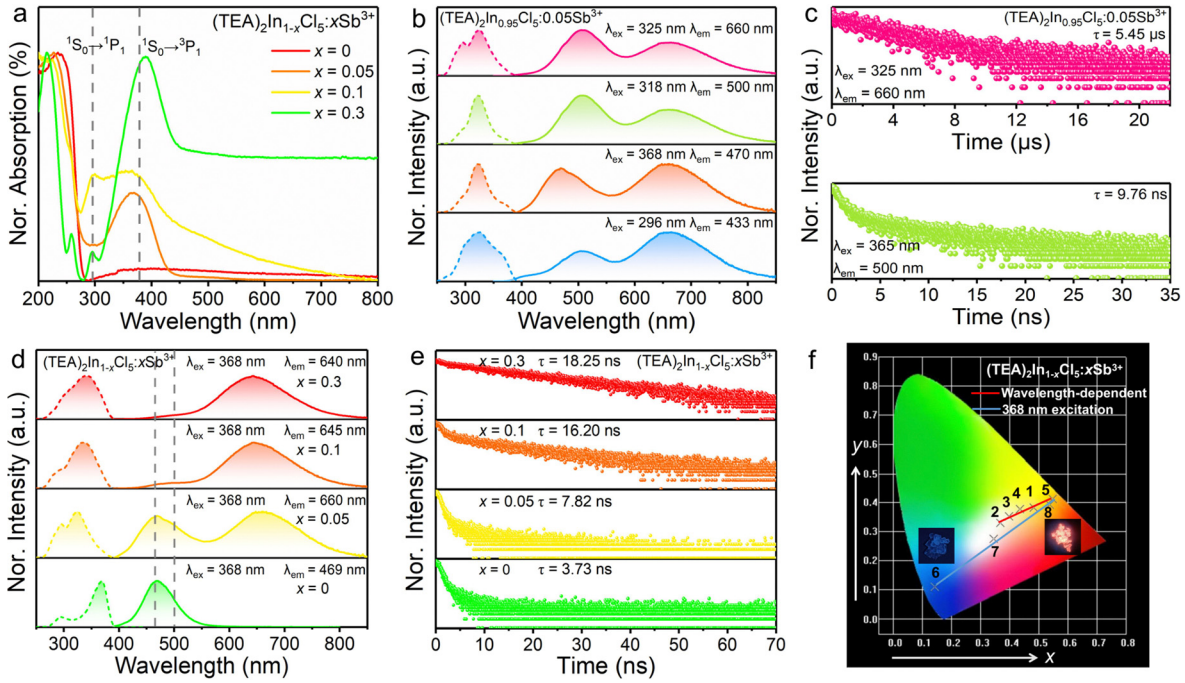

Fig. 6 (a) The normalized absorption spectra of $(TEA)_2In_{1-x}Cl_5:xSb^{3+}$. (b) Room-temperature PLE and PL spectra of $(TEA)_2In_{0.95}Cl_5:0.05Sb^{3+}$. (c) Room-temperature photoluminescence decay curves of $(TEA)_2In_{0.95}Cl_5:0.05Sb^{3+}$. (d) Room-temperature PLE and PL spectra of $(TEA)_2In_{1-x}Cl_5:xSb^{3+}$. (e) Room-temperature photoluminescence decay curves of $(TEA)_2In_{1-x}Cl_5:xSb^{3+}$ monitored at 470 nm. (f) CIE chromaticity diagram of compound $(TEA)_2In_{1-x}Cl_5:xSb^{3+}$ under different conditions with the lines drawn for the eye guide [red line, $(TEA)_2In_{0.7}Cl_5:0.3Sb^{3+}$ under excitation at different wavelengths at RT; blue line, $(TEA)_2In_{1-x}Cl_5:xSb^{3+}$ (x = 0, 0.05, 0.1, and 0.3) under 368 nm excitation].

changing the excitation energy provide a facile way to control the emission color from blue to orange-red and obtain warm white emission, which offers promising opportunities in the fields of constructing multicolor light-emitting devices.

To further explore the potential application of $(TEA)_2In_{0.7}Cl_5:0.3Sb^{3+}$ for solid-state lighting, a white light-emitting diode (WLED) was fabricated by combining our $(TEA)_2In_{0.7}Cl_5:0.3Sb^{3+}$ sample, the commercial blue phosphor $BaMgAl_{10}O_{17}:Eu^{2+}$ ($BAM:Eu^{2+}$), the commercial green phosphor $(Ba,Sr)_2SiO_4:Eu^{2+}$, and a UV-LED chip (365 nm, 1w). The device was driven using a 15 mA current at room temperature, and the corresponding luminescence spectrum and CIE diagram are plotted in Fig. 7a and b, respectively. The obtained results reveal that the CIE color coordinates are (0.362,0.343) with a color rendering index (CRI, R_a) of 85.1, a warm white light correlated color temperature (CCT) of 4306 K and a luminous efficacy (LE) of 33.11 lm W^{-1}. In addition, the PXRD patterns of $(TEA)_2InCl_5$ and $(TEA)_2InCl_5:Sb^{3+}$ for three months storage as well as the TGA of $(TEA)_2In_{0.95}Cl_5:0.05Sb^{3+}$ were measured to investigate the stability. $(TEA)_2InCl_5$ and $(TEA)_2InCl_5:Sb^{3+}$ keep almost pure phases after 90 days of exposure to air. Moreover, the $(TEA)_2In_{0.95}Cl_5:0.05Sb^{3+}$ crystal was stable up to 278 °C. These results indicate the high stability of $(TEA)_2InCl_5:Sb^{3+}$ which could be considered as an excellent candidate in the field of solid-state lighting (Fig. S6, ESI†).

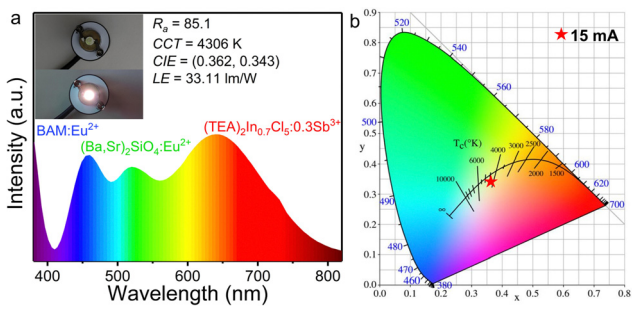

Fig. 7 (a) PL spectra of the WLED fabricated from our $(TEA)_2In_{0.7}Cl_5:0.3Sb^{3+}$ and commercial blue phosphor $BAM:Eu^{2+}$ as well as green phosphor $(Ba,Sr)_2SiO_4:Eu^{2+}$ on a near UV-LED chip (365 nm) at 15 mA driving current. (b) CIE chromaticity diagram of $(TEA)_2In_{0.7}Cl_5:0.3Sb^{3+}$ of the fabricated WLED.

Conclusions

In summary, a series of multi-color $(TEA)_2InCl_5:Sb^{3+}$ hybrids were prepared using a solution method, which show a typical 0D structure with five-coordinated $[InCl_5]^{2-}$ square pyramids and $[SbCl_5]^{2-}$ square pyramids separated by large organic cations. $(TEA)_2InCl_5$ possessed two kinds of emission centers, ascribed to the organic cations $(TEA)^+$ and STEs in the inorganic $[InCl_5]^{2-}$ square pyramids. After incorporating Sb^{3+} in $[InCl_5]^{2-}$ square pyramids, new dual-bands appeared at 500 nm and 660 nm owing to the singlet and triplet STEs in $[SbCl_5]^{2-}$ square pyramids, and the PLQY greatly increased from 30.11% to 78.85%. Furthermore, by adjusting the concentration of $[SbCl_5]^{2-}$ square pyramids or the excitation energy, warm white emission could be obtained. This work presents a new direction

towards designing environmentally friendly stable 0D metal halides and paves the way for modulating the luminescence performance *via* Sb^{3+} ion doping.

Conflicts of interest

There are no conflicts to declare.

Acknowledgements

This work is supported by the Beijing Natural Science Foundation (No. 2214068), the National Natural Science Foundation of China (No. 52202158 and 52202177), the Natural Science Foundation of Shanxi Province (No. 20210302124054), and the Scientific Research Ability Promotion Plan of Graduate Student of Beijing Technology and Business University in 2023.

Notes and references

1 M. Z. Li and Z. G. Xia, Recent progress of zero-dimensional luminescent metal halides, *Chem. Soc. Rev.*, 2021, **50**, 2626–2662.
2 D. Y. Li, Y. M. Sun, X. Y. Wang, N. N. Wang, X. Y. Zhang, C. Y. Yue and X. W. Lei, Zero-Dimensional Hybrid Indium Halides with Efficient and Tunable White-Light Emissions, *J. Phys. Chem. Lett.*, 2022, **13**, 6635–6643.
3 J. J. Luo, M. C. Hu, G. D. Niu and J. Tang, Lead-Free Halide Perovskites and Perovskite Variants as Phosphors toward Light-Emitting Applications, *ACS Appl. Mater. Interfaces*, 2019, **11**, 31575–31584.
4 M. Z. Li, J. Zhou, G. J. Zhou, M. S. Molokeev, J. Zhao, V. Morad, M. V. Kovalenko and Z. G. Xia, Hybrid Metal Halides with Multiple Photoluminescence Centers, *Angew. Chem., Int. Ed.*, 2019, **58**, 18670–18675.
5 J. Zhou, X. Y. Yun, C. Fang, D. H. Xu, X. Li, Y. Y. Cui and Z. C. Zhang, Ternary zero-dimensional hybrid metal halides with dual emission, *Mater. Today Chem.*, 2022, **23**, 100757.
6 B. B. Su and Z. G. Xia, Research Progresses of Photoluminescence and Application for Emerging Zero-dimensional Metal Halides Luminescence Materials, *Chin. J. Lumin.*, 2021, **42**, 733–754.
7 J. W. Lin, K. J. Liu, H. Ruan, N. Sun, X. Chen, J. Zhao, Z. N. Guo, Q. L. Liu and W. X. Yuan, Zero-Dimensional Lead-Free Halide with Indirect Optical Gap and Enhanced Photoluminescence by Sb Doping, *J. Phys. Chem. Lett.*, 2022, **13**, 198–207.
8 D. Chen, S. Q. Hao, G. J. Zhou, C. K. Deng, Q. L. Liu, S. L. Ma, C. Wolverton, J. Zhao and Z. G. Xia, Lead-Free Broadband Orange-Emitting Zero-Dimensional Hybrid $(PMA)_3InBr_6$ with Direct Band Gap, *Inorg. Chem.*, 2019, **58**, 15602–15609.
9 X. S. Zhang, X. X. Jiang, K. J. Liu, L. B. Fan, J. D. Cao, S. H. He, N. Wang, J. Zhao, Z. S. Lin and Q. L. Liu, Small Organic Molecular-Based Hybrid Halides with High Photoluminescence Quenching Temperature, *Inorg. Chem.*, 2022, **61**, 7560–7567.
10 L. Zhou, J. F. Liao, Z. G. Huang, J. H. Wei, X. D. Wang, H. Y. Chen and D. B. Kuang, Intrinsic Self-Trapped Emission in 0D Lead-Free $(C_4H_{14}N_2)_2In_2Br_{10}$ Single Crystal, *Angew. Chem., Int. Ed.*, 2019, **58**, 15435–15440.
11 J. W. Lin, Z. N. Guo, N. Sun, K. J. Liu, X. Chen, J. Zhao, Q. L. Liu and W. X. Yuan, High-efficiency red photoluminescence achieved by antimony doping in organic–inorganic halide $(C_{11}H_{24}N_2)_2[InBr_6][InBr_4]$, *J. Mater. Chem. C*, 2022, **10**, 5905–5913.
12 J. W. Lin, Z. N. Guo, K. J. Liu, N. Sun, J. D. Cao, X. Chen, J. Zhao, Q. L. Liu and W. X. Yuan, Tunable Bright White Light Emission with Ultra-High Color Rendering Index Induced by Trigonal Bipyramid Unit, *Adv. Opt. Mater.*, 2022, **11**, 2202304.
13 Q. Q. Ren, J. Zhang, M. S. Molokeev, G. J. Zhou and X. M. Zhang, Triplet–triplet energy transfer from Bi^{3+} to Sb^{3+} in zero-dimensional indium hybrids via a B-site co-doping strategy toward white-light emission, *Inorg. Chem. Front.*, 2022, **9**, 5960–5968.
14 C. M. Shi, J. L. Li, L. J. Xu, Y. Wu, H. L. Xuan, J. Y. Wang and Z. N. Chen, Methanol-induced luminescence vapochromism based on a Sb^{3+}-doped organic indium halide hybrid, *Sci. China Mater.*, 2022, **65**, 1876–1881.
15 B. Chen, Y. Guo, Y. Wang, Z. Liu, Q. Wei, S. X. Wang, A. L. Rogach, G. C. Xing, P. Shi and F. Wang, Multiexcitonic Emission in Zero-Dimensional $Cs_2ZrCl_6:Sb^{3+}$ Perovskite Crystals, *J. Am. Chem. Soc.*, 2021, **143**, 17599–17606.
16 J. P. Perdew, K. Burke and M. Ernzerhof, Generalized Gradient Approximation Made Simple, *Phys. Rev. Lett.*, 1996, **77**, 3865–3868.
17 P. E. Blochl, Projector augmented-wave method, *Phys. Rev. B*, 1994, **50**, 17953–17979.
18 G. Kresse and D. Joubert, From ultrasoft pseudopotentials to the projector augmented-wave method, *Phys. Rev. B*, 1999, **59**, 1758–1775.
19 S. Grimme, J. Antony, S. Ehrlich and H. Krieg, A consistent and accurate ab initio parametrization of density functional dispersion correction (DFT-D) for the 94 elements H-Pu, *J. Chem. Phys.*, 2010, **132**, 154104.
20 S. Grimme, S. Ehrlich and L. Goerigk, Effect of the Damping Function in Dispersion Corrected Density Functional Theory, *J. Comput. Chem.*, 2011, **32**, 1456–1465.
21 V. Wang, N. Xu, J. C. Liu, G. Tang and W. T. Geng, VASPKIT: A user-friendly interface facilitating high-throughput computing and analysis using VASP code, *Comput. Phys. Commun.*, 2021, **267**, 108033.
22 M. Y. Li, J. W. Lin, N. Wang, K. J. Liu, L. B. Fan, Z. N. Guo, W. X. Yuan, J. Zhao and Q. L. Liu, Synthetic-Method-Dependent Antimony Bromides and Their Photoluminescent Properties, *Inorg. Chem.*, 2022, **61**, 15016–15022.
23 Y. Wu, C. M. Shi, L. J. Xu, M. Yang and Z. N. Chen, Reversible Luminescent Vapochromism of a Zero-Dimensional Sb^{3+}-Doped Organic-Inorganic Hybrid, *J. Phys. Chem. Lett.*, 2021, **12**, 3288–3294.

24 J. P. Perdew and M. Levy, Physical Content of the Exact Kohn-Sham Orbital Energies: Band Gaps and Derivative Discontinuities, *Phys. Rev. Lett.*, 1983, **51**, 1884–1887.
25 R. W. Godby, M. Schluter and L. J. Sham, Trends in self-energy operators and their corresponding exchange-correlation potentials, *Phys. Rev. B*, 1987, **36**, 6497–6500.
26 Y. Y. Zhang, S. Y. Yuan, Y. X. Yuan, Y. K. Bao, Q. Ran, E. M. Liu, J. D. Fan and W. Z. Li, Alleviation of π–π* Transition Enabling Enhanced Luminescence in Emerging $TpyInCl_x$ (x = 3, 5) Perovskite Single Crystals, *Adv. Opt. Mater.*, 2021, **10**, 2102041.
27 H. Fattal, T. D. Creason, C. J. Delzer, A. Yangui, J. P. Hayward, B. J. Ross, M. H. Du, D. T. Glatzhofer and B. Saparov, Zero-Dimensional Hybrid Organic-Inorganic Indium Bromide with Blue Emission, *Inorg. Chem.*, 2021, **60**, 1045–1054.
28 Z. Y. Li, G. M. Song, Y. Li, L. Wang, T. L. Zhou, Z. S. Lin and R. J. Xie, Realizing Tunable White Light Emission in Lead-Free Indium(III) Bromine Hybrid Single Crystals through Antimony(III) Cation Doping, *J. Phys. Chem. Lett.*, 2020, **11**, 10164–10172.
29 J. H. Wei, J. F. Liao, L. Zhou, J. B. Luo, X. D. Wang and D. B. Kuang, Indium-antimony-halide single crystals for high-efficiency white-light emission and anti-counterfeiting, *Sci. Adv.*, 2021, **7**, 3989.
30 J. Zhou, X. M. Rong, M. S. Molokeev, Y. L. Wang, X. Y. Yun, D. H. Xu and X. Li, Alloying Cs+ into Rb2ZrCl6:Te^{4+} toward highly efficient and stable perovskite variants, *Mater. Chem. Front.*, 2021, **5**, 4997–5003.
31 B. Bai, P. P. Dang, D. Y. Huang, H. Z. Lian and J. Lin, Broadband Near-Infrared Emitting $Ca_2LuScGa_2Ge_2O_{12}:Cr^{3+}$ Phosphors: Luminescence Properties and Application in Light-Emitting Diodes, *Inorg. Chem.*, 2020, **59**, 13481–13488.
32 Z. X. Wu, X. X. Han, Y. Y. Zhou, K. Xing, S. Cao, L. Chen, R. S. Zeng, J. L. Zhao and B. S. Zou, Efficient broadband near-infrared luminescence of Cr^{3+} doped fluoride K_2NaInF_6 and its NIR-LED application toward veins imaging, *Chem. Eng. J.*, 2022, **427**, 131740.
33 X. F. Zhou, W. Y. Geng, J. Y. Li, Y. C. Wang, J. Y. Ding and Y. H. Wang, An Ultraviolet–Visible and Near-Infrared-Responded Broadband NIR Phosphor and Its NIR Spectroscopy Application, *Adv. Opt. Mater.*, 2020, **8**, 1902003.
34 C. Tong, Q. L. Wei, R. S. Zeng, S. Cao, J. L. Zhao and B. S. Zou, Efficient Energy Transfer in Te^{4+}-Doped Cs_2ZrCl_6 Vacancy-Ordered Perovskites and Ultrahigh Moisture Stability via A-Site Rb-Alloying Strategy, *J. Phys. Chem. Lett.*, 2021, **12**, 1829–1837.
35 C. Fang, J. K. Yang, G. J. Zhou, Z. C. Zhang, Y. J. Mao, X. Y. Yun, L. B. Liu, D. H. Xu, X. Li and J. Zhou, Energy transfer from self-trapped excitons to rare earth ions in Cs_2ZrCl_6 perovskite variants, *J. Mater. Chem. C*, 2023, **11**, 1095–1102.
36 J. Zhou, X. Y. Yun, R. Y. Wang, D. H. Xu and X. Li, Self-trapped exciton to dopant energy transfer in Sb^{3+}-doped Cs_2ZrCl_6 perovskite variants, *Mater. Chem. Front.*, 2021, **5**, 6133–6138.
37 G. M. Song, M. Z. Li, S. Z. Zhang, N. Z. Wang, P. F. Gong, Z. G. Xia and Z. S. Lin, Enhancing Photoluminescence Quantum Yield in 0D Metal Halides by Introducing Water Molecules, *Adv. Funct. Mater.*, 2020, **30**, 2002468.